HHS Public Access

Author manuscript

IEEE Access. Author manuscript; available in PMC 2022 October 20.

Published in final edited form as:

IEEE Access. 2022 ; 10: 105074–105083. doi:10.1109/access.2022.3210590.

Use of the Fully Spectroscopic Pixelated Cadmium Telluride Detector for Benchtop X-Ray Fluorescence Computed Tomography

SANDUN JAYARATHNA[1], **HEM MOKTAN**[1], **SANG HYUN CHO**[1,2]

[1]Department of Radiation Physics, The University of Texas MD Anderson Cancer Center, Houston, TX 77030, USA

[2]Department of Imaging Physics, The University of Texas MD Anderson Cancer Center, Houston, TX 77030, USA

Abstract

In this work, we integrated a commercially-available fully-spectroscopic pixelated cadmium telluride (CdTe) detector system as a two-dimensional (2D) array detector into our existing benchtop cone-beam x-ray fluorescence computed tomography (XFCT) system. After integrating this detector, known as High-Energy X-ray Imaging Technology (HEXITEC), we performed quantitative imaging of gold nanoparticle (GNP) distribution in a small animal-sized phantom using our benchtop XFCT system. Owing to the upgraded detector component within our benchtop XFCT system, we were able to conduct this phantom imaging in an unprecedented manner by volumetric XFCT scans followed by XFCT image reconstruction in 3D. The current results showed that adoption of HEXITEC, in conjunction with a custom-made parallel-hole collimator, drastically reduced the XFCT scan time/dose. Compared with the previous work performed with our original benchtop XFCT system adopting a single crystal CdTe detector, the currently observed reduction was up to a factor of 5, while achieving comparable GNP detection limit under similar experimental conditions. Overall, we demonstrated, for the first time to the best our knowledge, the feasibility of benchtop XFCT imaging of small animal-sized objects containing biologically relevant GNP concentrations (on the order of 0.1 mg Au/cm^3 or 100 parts-per-million/ppm), with the scan time (on the order of 1 minute)/x-ray dose (on the order of 10 cGy) that are likely meeting the minimum requirements for routine preclinical imaging applications.

INDEX TERMS

X-ray fluorescence; X-ray fluorescence computed tomography; CdTe detector; HEXITEC; gold nanoparticle; quantitative imaging

Corresponding author: Sang Hyun Cho (scho@mdanderson.org).

I. INTRODUCTION

X-ray fluorescence (XRF) computed tomography (XFCT) is a powerful spectroscopic quantitative imaging technique, traditionally implemented with monochromatic synchrotron sources [1], [2], [3], [4]. Over the last decade, there has been a growing interest in implementing XFCT with ordinary polychromatic sources on a benchtop setting, as benchtop XFCT, resulting from such an implementation, may allow for quantitative imaging of metal-based nanoparticles such as gold nanoparticles (GNPs) during preclinical investigations of various diagnostic/therapeutic applications of such nanoparticles [5], [6], [7]. Typical experimental benchtop XFCT setups are consisted of polychromatic x-ray sources configured to offer various incident (cone-, pencil-, and sheet-) beam geometries as well as x-ray detectors coupled with parallel-hole, pinhole, and multi-pinhole collimators [8], [9], [10], [11], [12]. Early benchtop XFCT setups often adopted an energy-resolving single-crystal (or single-pixel) solid state (e.g., cadmium telluride) detector that needed to be translated (horizontally or vertically) with respect to the imaging object or vice versa to acquire the full projection data set. Although generally well suited for benchtop XFCT, such a detector, regardless of the incident beam geometry, requires a long scanning time due to the hardware translation. Depending on the incident beam geometry, the detector translation also imposes a large imaging dose on the object. One way to overcome these difficulties is to use an array of single crystal detectors or a pixelated detector.

In recent years, there have been some reports of using pixelated photon counting detectors for benchtop XFCT or XRF mapping, especially in conjunction with pin-hole collimators under the fan/sheet-beam geometry [12], [13], [14]. While somewhat successful in addressing the difficulties mentioned above, the investigations conducted with such detectors also revealed other types of challenges, most notably the reduced system sensitivity (or material detection limit), compared with the use of a single crystal detector. In benchtop XFCT, the system sensitivity is closely related with the detector energy resolution because XRF signals must be extracted from the measured photon spectra that contain both XRF peaks and the Compton scatter background. In general, the photon spectra acquired with high energy resolution can facilitate the extraction of XRF signals. Thus, pixelated detectors providing high energy resolution/full spectrum are preferred over those providing relatively low energy resolution/limited energy bins. As pointed out elsewhere [15], however, it remains to be seen whether or not high energy resolution pixelated detectors can help avoid or mitigate the issues noted with relatively low energy resolution pixelated detectors, especially under the typical operating conditions of benchtop XFCT.

To investigate the possibility of adopting a high energy resolution pixelated detector for benchtop XFCT, we conducted an experimental study [16] where the characteristics of a commercially available pixelated cadmium telluride (CdTe) detector system, known as HEXITEC (High-Energy X-ray Imaging Technology) [17], [18], were determined using our experimental benchtop cone-beam XFCT system and GNP-loaded phantoms. Specifically, we determined the energy resolution of HEXITEC (~1 keV, FWHM-full width at half maximum) around two gold Kα XRF peaks (~68 keV) and found a charge-sharing discrimination algorithm was the most effective, in terms of improving the energy resolution of acquired photon spectra. In addition, we developed what we termed as a pixel-by-pixel

spectrum merging algorithm, which can allow for acquisition of statistically stable photon spectra (in conjunction with parallel-hole detector collimators) under the typical operating conditions of benchtop XFCT.

Upon completion of the detector characterization study described above, we proceeded to fully deploy HEXITEC (coupled with a custom-made 2D collimator) into our experimental benchtop XFCT system. Our primary aim for the current study was then to demonstrate the ultimate feasibility of performing benchtop XFCT of animal-sized objects containing GNP-loaded inserts using the revamped benchtop XFCT system. Especially, we focused on investigating this feasibility, while meeting the imaging dose (e.g., <~40 cGy) and scan time (e.g., <~1 hour) constraints that would be acceptable for preclinical imaging [9], [15]. We also showed an immediate consequence of parallel spectral data acquisition using a 2D pixelated detector - imultaneous XFCT imaging of multiple axial slices of the imaging object. To the best of our knowledge, the current investigation was the first successful experimental work that addressed all these aspects together, highlighting the feasibility for routine applications. Here we present the details of our work, along with some discussion regarding the remaining challenges for building a practical benchtop XFCT system.

II. METHODS

A. GNP SOLUTIONS AND IMAGING PHANTOMS

Various concentrations of GNP solutions (0.03–1.0 mg Au/cm^3) were made by a sequential dilution method from a commercially available stock solution (40 mg Au/cm^3, AuroVist 15 nm by Nanoprobes Inc, Yaphank, NY, USA) combined with phosphate-buffered saline.

Two types of phantoms were used to suspend GNP solutions during the irradiation: one was for calibration, consisting of 12-mm-diameter plastic tubes filled with selected GNP concentrations for determining the lowest detectable GNP concentration with the current benchtop XFCT system. The other was for imaging, consisting of a 3-cm-diameter and 3-cm-high polymethyl methacrylate (PMMA)-made cylinder with three GNP-loaded cylindrical holes (6 mm diameter/15 mm depth each), which was also used in our previous studies [9], [11], [19]. Each hole of the imaging phantom was filled with 0.1, 0.3, and 0.5 mg Au/cm^3 GNP solution.

B. EXPERIMENTAL BENCHTOP XFCT SYSTEM

The latest version of our experimental benchtop cone-beam XFCT system is shown in Fig. 1. The irradiation component of the system consists of an industrial high-power tungsten target x-ray source (COMET MXR-160/22) that operates at 125 kVp and 24 mA with a 5-mm focal spot size, coupled to a cone-beam collimator (made of 5-cm-thick lead) with a 1-cm-diameter inlet and 2-cm-diameter outlet. The collimator outlet was fused to a 1.8-mm tin filter to harden the incident x-ray spectrum for optimal production of gold K-shell XRF photons from GNPs [9]. The irradiation component produces a ~3-cm-diameter cone-beam at the imaging isocenter, located at 15 cm from the x-ray source.

A rotational stage (PRMTZ8 ThorLabs, Inc., Newton, NJ, USA) in the system supports the phantoms. It remains stationary during the calibration mode but allows for the rotation of the

phantom during the imaging mode. The center of the rotational stage is the isocenter of the imaging system.

The XRF detection component of the system consists of HEXITEC housed inside the shielded chamber and coupled with the detector collimator at 90° with respect to the incident beam direction and aligned toward the isocenter. The component was placed on top of a linear stage (NRT150, ThorLabs, Inc.) so that horizontal translations could be applied during data acquisition if needed. The isocenter-to-detector distance was fixed at 10 cm.

Another component of the current XFCT system (not shown in Fig. 1, as it was not used for this work) is a flat panel detector (Dexela 1207, PerkinElmer, Inc., Waltham, MA, USA) that can be used for simultaneous or sequential transmission CT with XFCT. More details about this component can be found elsewhere [8].

Software developed in-house (with MATLAB) was used to control the rotational stage as well as the linear stage during data acquisition.

C. HEXITEC DETECTOR SYSTEM

HEXITEC is manufactured for spectroscopic x-ray detection with a 2D pixelated sensor in the energy range of 3 to 200 keV. The system can operate at room temperature without a dedicated cryogenic cooling system. The CdTe sensor (2 cm × 2 cm) and readout electronics are inside of an aluminum casing (21 cm × 5 cm × 5 cm). The CdTe sensor has a total of 6400 (80 × 80) individual pixels (pixel pitch of 250 μm). Each pixel can accumulate the energy deposition in 800 bins where the final x-ray spectrum is tabulated by combining multiple frames (frame rate ~9 kHz). The recommended operating bias-voltage is −500 V. The software component associated with HEXITEC comes with a built-in dynamic 2D display of the sensor area where output data can be saved in a proprietary binary format (.hxt and .bin). These data files can be used for offline data analysis (spectrum processing, charge sharing correction, etc.) without repeating the experiment.

D. 2D PARALLEL-HOLE DETECTOR COLLIMATOR

The detector was coupled to a 2D parallel-hole collimator, fabricated from stainless steel. The collimator consisted of 49 individual parallel holes, with a 2-mm hole diameter and 1-mm septum thickness (Fig. 2a). The 49 holes were distributed in 7 × 7 rows and columns in such a way that they covered the 2 cm × 2 cm field of view (FOV) of the CdTe sensor.

The overall dimensions of the collimator were 3.5 cm × 3.5 cm × 5 cm (Fig. 2b). The selection of stainless steel as the collimator material was to avoid any XRF production from the collimator material, which could interfere with gold Kα1 and Kα2 (68.8 and 67.0 keV, respectively) XRF photons.

The selection of the aperture diameter was to increase the system sensitivity, as demonstrated in our previous experimental study [9]. The collimator septum thickness was estimated to be 1 mm by the approach described below, to avoid XRF cross-interference between different holes during the data acquisition. The minimum collimator septum thickness (t) can be calculated as follows [20]:

$$t \geq \frac{6d/\mu}{L - (3/\mu)}$$

where $\mu = 2.927\ \text{cm}^{-1}$ is the liner attenuation coefficient of steel at 100 keV; L, d are the length and diameter of collimator holes, respectively. Substituting these values for the equation gives t ≥ 1.03 mm; thus, to accommodate engineering efficiency and to cover the maximum field of view, this was taken to be 1 mm. Since the XRF energy window of interest for gold resides far below 100 keV, this design ensures that no XRF signal extracted for the final analysis originated from outside the corresponding collimated region.

E. DETECTOR SHIELDING CHAMBER

The shielding chamber for HEXITEC served for the two following purposes: first to protect the sensitive electronics of the detector and second to avoid unwanted scatter x-rays getting into the detector sensor elements. The frontal part of this shielding chamber was made of stainless steel (Fig. 2c). The thickness of the base plate was 2.5 cm. The frontal part also had a protruding structure with an opening of 3.5 cm × 3.5 cm × 5.0 cm, where various types of collimators (up to 5 cm in thickness) could be inserted. The top, two sides, and bottom of the shielding chamber were covered with lead plates (~1 cm thick each) to avoid the transmission of roof and wall scattered radiation from the high-power x-ray source.

F. BEAM ALIGNMENTS FOR IMAGING

The height from the tabletop to the x-ray source center was fixed and taken as the origin (all distances measured with reference to this point). The source collimator, phantom, and detector centers were all placed at the same height in order to have a coplanar imaging platform. A pointing laser was used to align the phantom center to the x-ray source origin along the incident beam direction. A second laser was then used at 90° to the first laser to align the phantom center to the center of the detector collimator (row = 4, column = 4 in the collimator (Fig. 2d)).

G. DATA ACQUISITION

1) INPUT/OUTPUT CONTROL OF HEXITEC—HEXITEC has a control software package compatible with the Windows operating system. The data I/O was established via a high-speed GigE-Ethernet cable. The operating bias-voltage was set to −500 V. During the operation, the internal temperature was automatically adjusted to ~27°C. The spectrum channel numbers were converted to energy bins by using a built-in energy calibration protocol in the HEXITEC software; specifically, 800 energy bins were used over the 0–128 keV energy range with a bin resolution of 0.16 keV. An energy calibration protocol for HEXITEC was following the previous study [17] using two radioisotope sources (Am-241 with a photopeak at 59.5 keV and Co-57 with photopeaks at 122 and 136 keV). Two types of binary files were created at the end of data acquisition. The first file was used to read the per-pixel energy spectra after all data frames were combined after the scanning and to visualize the 2D-sensor elements; the second file was used to post-process the data to correct for small pixel charge sharing effects.

2) PHANTOM IRRADIATION/XFCT SCAN—Each calibration phantom was irradiated for 5 and 10 s (45×10^3 and 90×10^3 frames, respectively). Once the calibration phantom was fixed at the isocenter, it was confirmed to align the central collimator hole with the mid-section of the suspended GNP column inside the phantom. This ensured a good XRF signal acquisition around the central collimated region. Each calibration phantom for a given concentration was irradiated 3 times to estimate the statistical uncertainty.

For XFCT scan, the imaging phantom (3 cm in diameter) was greater than the 2-cm FOV of the sensor area of HEXITEC. Thus, at least one horizontal detector translation was necessary to cover the entire imaging phantom. This was achieved by first scanning the right side of the phantom for 5 and 10 s, and then translating the detector to the left side and scanning the phantom for another 5 and 10 s, and finally combining the two individual output files (.hxt) for post processing. Although the total scan time per projection became 10 and 20 s from this approach, the number of frames acquired in the HEXITEC was the same (45×10^3 and 90×10^3) after combining the outputs, which was compatible with the settings used in the calibration phantom irradiation. Once the data acquisition was finished for both sides, the phantom was rotated by 12° and the procedure was repeated from 0° to 348°.

3) XRF SIGNAL EXTRACTION AND CORRECTIONS—Software developed in-house (Python 3.5) was used to extract the x-ray spectra detected from HEXITEC. The pixel-level charge sharing correction algorithm was used before processing the data further. HEXITEC software has two such correction techniques, namely, charge sharing discrimination (csd) and charge sharing addition (csa) [18, 21]. For XFCT, csa was found to be better than csd, in terms of enhancing the XRF detection sensitivity [16] and was therefore used in the current investigation. Note both csd and csa can be applied offline after the scanning data have accumulated, which allows the user to acquire the spectral data in any correction mode without losing the original real-time data. Thus, they were applied offline in the current study to facilitate our analysis.

Owing to the smaller detector pixel pitch, the per-pixel spectra from 5 and 10 s irradiation time were statistically unstable for the extraction of XRF signals from the Compton scatter background. Thus, per-pixel energy spectra within each collimated region (over a 10 × 10-pixel area) were combined to obtain statistically stable composite spectra, following the procedure (known as pixel-by-pixel spectrum merging) developed in our previous study [16].

After the XRF/scatter spectra were acquired, they were corrected for CdTe detection efficiency and XRF counts were then extracted from the corrected XRF/scatter spectra, applying a deconvolution-based method developed in our previous study [19]. XRF counts under gold Kα1 and Kα2 peaks were summed to obtain the net XRF counts. Consistent with the previous studies [9, 19], XRF counts of less than 1.96 σ_b (σ_b = standard deviation of the background at the 95% confidence level) were considered statistically insignificant.

4) ESTIMATION OF IMAGING DOSE—The x-ray dose during the XFCT scan was estimated using the ionization-chamber measured dose rate under the current experimental conditions, following the procedure detailed elsewhere [9]. Briefly, ionization chamber

measurements were performed with a standard Farmer-type ionization chamber (N30013, PTW Freiburg) and an electrometer (DOSE 1, IBA Dosimetry GmbH) using the same PMMA-made dosimetry phantom as used previously. The AAPM TG-61 formalism [22] was applied to correct raw readings from ionization chamber measurements.

III. RESULTS

A. REAL TIME 2D IMAGES FROM HEXITEC

A useful feature of the HEXITEC software is a real-time 2D display of the sensor area during data acquisition. For the current benchtop XFCT setup, it was used to further align the detector collimator toward the imaging phantom. Figs. 3a and 3b show the multi-frame 2D images acquired during the 5 s scanning of the calibration and imaging phantoms, respectively. In both images, the collimator holes were clearly visible over the entire window corresponding to the sensor area. The color bars represent the number of photons that reached the detector and accumulated within the energy window of 3–125 keV. It can be seen from the images that the collimated regions (high-intensity pixel clusters) were not overlapped, which justified the currently chosen collimator design parameters (aperture diameter and septum thickness) and isocenter-to-detector distance (10 cm).

B. IMAGE RESOLUTION

The effective diameter of each collimated region seen through the sensor area was ~2.8 mm. Thus, 2.8 mm was considered the spatial resolution achievable from the current parallel-hole detector collimation along both the x and y directions. To better quantify the spatial resolution, line profiles were acquired along the x-/y-axes through the central pixel of the sensor area. Fig. 4a shows the profiles for y = 38, 39, 40, 41, and 42, where 7 distinct spikes are visible for each collimated region with a corresponding effective width of ~2.5 mm (nearly equal to the spatial resolution of 20 mm/7 ~2.8 mm).

Fig. 4b demonstrates the same corresponding profiles along the x-axis, where 7 distinct spikes are visible with the same estimated effective width. These suggested a spatial resolution reduction by a factor of ~10 (2.8 mm/250 μm).

As explained earlier, due to the 3-cm diameter of the imaging object, one translation was needed for the current analysis, and output files were merged side by side (for left scan + right scan) for each rotation (Fig. 5). As shown, instead of 49 parallel holes, 77 such holes were obtained, mimicking HEXITEC with a larger sensor area coupled to a 11 × 7 stainless-steel parallel-hole collimator. Thus, the effective width of the object that could be imaged became 11 × 2.8 mm ~ 30.8 mm (>3 cm), where 2.8 mm is the spatial resolution of the system.

C. XRF SIGNAL EXTRACTION

The spectrum obtained after charge sharing correction and pixel-by-pixel spectrum merging followed by efficiency correction is illustrated in Fig. 6 for the calibration phantom filled with GNPs at 0.05 mg Au/cm^3.

The red line shows the modeled Compton background and the XRF peaks extracted using our deconvolution-based algorithm [19] are shown at the bottom. To obtain the net gold XRF counts, the extracted peaks were integrated over the energy window of 65–71 keV; this region of interest is demarcated by two vertical lines in Fig. 6.

D. CALIBRATION CURVE AND DETECTION LIMIT OF THE SYSTEM

The XRF signal extraction procedure was repeated for GNP solutions at 0.03–1.0 mg Au/cm^3 concentrations to obtain the calibration curve. The obtained calibration curves (net XRF signals vs GNP concentrations) are shown in Fig. 7 a and b for data acquisition time of 5 and 10 s, respectively. The data were fitted to show the linearity. As illustrated in Fig 7 c and d, no statistically meaningful net XRF signals (beneath 1.96σ from the background) could be extracted from the samples of less than 0.05 mg Au/cm^3 for 5 s acquisition time and 0.03 mg Au/cm^3 for 10 s acquisition time. Thus, with the current benchtop XFCT configuration, the detection limit achievable with 5 and 10 s data acquisition time was estimated to be 0.05 mg Au/cm^3 and 0.03 mg Au/cm^3, respectively.

E. PROJECTION DATA

For XFCT image reconstruction, projection sinograms were calculated for each imaging slice corresponding to the collimator row (the first collimator row from the top as slice 1, the second collimator row from the top as slice 2, etc.) by using the net XRF photon counts extracted from gold Ka_1 and Ka_2 peaks for data acquisition time of 5 s (Fig. 8a–e) and 10 s (Fig. 8f–j). Here the y axis showed the number of detector elements, and the x axis showed the angle of rotations. Parallel beam sinograms containing extracted net XRF counts for each collimator slice were stored in a single HDF5 (Hierarchical Data Format) file and saved for XFCT image reconstruction.

F. AXIAL IMAGE RECONSTRUTION

The axial XFCT images were reconstructed by using a filtered back projection algorithm (MATLAB, The Mathworks, Natick, MA). During the reconstruction, additional adjustments were done for attenuation of gold XRF signals inside the phantom and attenuation of the excitation beam, using a Compton scatter-based attenuation correction algorithm, as in our previous studies [8, 23]. The reconstructed XFCT images were further filtered by using a Gaussian filter. For better visualization, the reconstructed axial slices were interpolated by using linear interpolation. The reconstructed counts in each pixel were converted to GNP concentration by using the calibration curve. After the conversion, thresholding of pixels having a GNP concentration of <0.03–0.05 mg Au/cm^3 were applied since no concentration below the detection limit should give any statistically meaningful information. The reconstructed axial XFCT images are shown for data acquisition time of 5 s (Fig. 9a–e) and 10 s (Fig. 9f–j) respectively.

G. GNP CONCENTRATION FROM RECONSTRUCTED IMAGES

Once the reconstructed images corresponding to 5 and 10 s scan time became available, the GNP concentrations from the reconstructed images were obtained by calculating the mean values of ROIs inside the imaging phantom corresponding to the GNP-loaded regions and

the associated standard deviations. In Fig. 10, calculated GNP concentrations were plotted against the actual concentrations.

For clarity of presentation, GNP concentrations calculated for all 5 XFCT slices were shown as a box plot. The average reconstructed GNP concentrations for all axial slices in 5 s scan time were found to be 0.085 ± 0.013, 0.287 ± 0.029, and 0.497 ± 0.012. On the other hand, for 10 s scan time, the average reconstructed concentrations were found to be 0.108 ± 0.009, 0.302 ± 0.010 and 0.507 ± 0.007. Thus, the percent standard deviation was maximum, ~15% (0.1 to 0.085 mg Au/cm^3), for 0.1 mg Au/cm^3 at 5 s and decreased to 8% (0.1 to 0.108 mg Au/cm^3), when the data acquisition time increased to 10 s. For higher GNP concentrations, the average values derived from the reconstructed images deviated less than 5% for both 5 and 10 s scan time.

H. CONTRAST-TO-NOISE RATIO IN RECONSTRUCTED IMAGES

Although the GNP-loaded regions in reconstructed XFCT images were qualitatively visible, a quantitative analysis was performed using the contrast-to-noise ratio (CNR), a function of the mean signal and associated standard deviation for each GNP-loaded region:

$$CNR = \frac{S_{ROI} - S_{BKG}}{\sqrt{\left(\sigma^2_{ROI} + \sigma^2_{BKG}\right)}}$$

where S_{ROI} is the mean pixel value of an ROI within a GNP-loaded region; S_{BKG} is the mean pixel value of the center of the phantom (a background region where no GNP-induced XRF can be generated); σ^2_{ROI} and σ^2_{BKG} are the associated square of the standard deviations. As in our pervious study [24] and based on the Rose criterion [25], the cutoff threshold value of 3 was selected for the CNR. For values <3, GNPs were considered undetectable. As depicted in Fig. 11, large CNR values, up to ~14, were observed for some axial slices in the reconstructed XFCT images, especially those based on the 10 s acquisition time.

CNR values for the GNP-loaded regions within the current imaging phantom were generally above 3, although some parts (i.e., axial slice 1–2) of the region filled with the lowest GNP concentration of 0.1 mg Au/cm^3 were shown with CNR values below 3 for the 5 s acquisition time. The average CNR values for 0.1,0.3,0.5 mg Au/cm^3 for all axial slices in 5 s scan time were found to be 3.028 ± 0.610, 6.047 ± 0.326 and 8.113 ± 0.509, respectively. For 10 s scan time, the average CNR values were found to be 4.948 ± 0.363, 11.047 ± 0.326 and 13.913 ± 0.449 for 0.1,0.3,0.5 mg Au/cm^3 respectively, which shows the effectiveness of increasing scan time (i.e., x-ray dose) to get better quality reconstructed images.

I. RECONSTRUCTED XFCT IMAGE IN 3D

Once the axial images were reconstructed, they were stacked along the long axis (+Z) of the phantom to obtain the reconstructed images in 3D. The reconstructed 3D image matrix was saved, and the projection images along the proper planes were acquired as shown in Fig. 12. The coronal plane was defined in ZY and the sagittal plane was defined in ZX coordinate, respectively. As seen, the regions loaded with relatively high GNP concentrations (0.3–0.5 mg Au/cm^3) were well reconstructed (sagittal plane projection in Fig 12). On the other hand,

the region loaded with GNPs at 0.1 mg Au/cm^3 suggests the difficulty of reconstructing the regions loaded with low GNP concentrations based on the 5 s acquisition time. Note, although not shown in Figure 12 due to close similarity, the reconstructed images based on the 10s acquisition time showed more clearly the region loaded with GNPs at 0.1 mg Au/cm^3 region. Also, all GNP-loaded regions showed some local variation in the GNP concentration, especially in the reconstructed images based on the 5 s acquisition time (as shown by the green arrows).

J. XFCT IMAGING DOSE AND SCAN TIME

The dose rate determined from the current work was 21.3 cGy/min at the isocenter. For a complete XFCT scan of the current imaging phantom with 5 s acquisition time per projection, therefore, a total dose per projection was calculated to be 1.775 cGy (21.3 cGy/min × 5 s). Similarly, with 10 s acquisition time per projection, a total dose per projection became 3.55 cGy. Accordingly, the total XFCT imaging dose with 29 angular rotations (30 angular positions) and 1 horizontal translation (2 translational positions) of HEXITEC was 106.5 and 213 cGy for 5 and 10 s acquisition time, respectively. If a horizontal detector translation was not necessary, the total XFCT imaging dose from the current work would become ~53 and ~107 cGy for 5 and 10 s acquisition time, respectively. Note, while it could not be achievable during the current work, this scenario (i.e., no horizontal detector translation) is readily achievable with a newer version of HEXITEC [26] providing a larger FOV or XFCT scanning of smaller objects that can be within the current FOV of HEXITEC.

Similar to the XFCT imaging dose, the total XFCT scan time was found to be 300 s (or 5 min) and 600 s (or 10 min) for the scans with 5 and 10 s acquisition time per projection, respectively. Compared with the results from our previous study performed under the same experimental conditions (except for the use of a single crystal CdTe detector) [9], the currently achieved XFCT imaging dose and scan time were remarkable, suggesting almost a factor of 5 reduction. This was an immediate consequence of making only one horizontal detector translation during the current work (vs. 10 such translations in the previous work) to scan the entire phantom. Further reduction (i.e., additional 5 folds) in the XFCT imaging dose and scan time would also be immediately achievable, if no horizontal detector translation was necessary.

IV. DISCUSSION

The focus of the current work was to show the feasibility and strength of integrating a fully spectroscopic pixelated HEXITEC detector into an experimental benchtop XFCT system. As shown, this integration allowed for parallel detection of XRF photons, resulting in drastic reduction in the XFCT imaging dose/scan time as well as enabling quantitative imaging of the 3D distribution of GNPs inside a small animal–sized object.

Compared to a few earlier versions of our experimental benchtop XFCT setup and related investigations, several novel approaches from both hardware and software perspectives were adopted in this work. First, a new custom-made 2D stainless-steel parallel-hole collimator was introduced to enable the detection of XRF photons with a pixelated detector,

as the vertical and/or horizontal translations of a single crystal detector were no longer necessary. Second, a previously developed pixel-by-pixel spectrum merging technique was extended to handle the spectral data acquired through a 2D parallel-hole collimator. This approach, in conjunction with our deconvolution-based XRF signal extraction algorithm, was essential to achieve the currently reported system sensitivity, especially with 5 s of data acquisition time at each projection. As reported in our recent study [16], HEXITEC provided somewhat worse energy resolution under the current measurement conditions than that reported previously. Nonetheless, when combined with the approaches mentioned above, it allowed for fast enough imaging of a given GNP-loaded object while providing the system sensitivity comparable to that achievable with a single crystal CdTe detector under the similar experimental conditions [9].

The spatial resolution of the current imaging setup was limited by incorporation of a 2-mm parallel-hole collimator. Despite this limitation, the use of the current collimator, in conjunction with a pixelated detector, was a reasonable compromise, given the reduced system sensitivity from the use of other types of detector collimators (e.g., pinhole collimator) potentially providing higher image resolution [27]. In the case of a single crystal CdTe detector, the image resolution could also be improved by translating it in finer steps (e.g., less than 2 mm), but the scan time will become prohibitively long. In principle, a custom 1D- or 2D-array of single crystal CdTe detectors can be used, instead of pixelated detectors. As explained elsewhere [15], however, such an array cannot be easily deployed into a benchtop XFCT system on a relatively small footprint such as the one described in this study for preclinical imaging purposes. Thus, the use of a parallel-hole collimator, in conjunction with a pixelated detector, can be well justified, especially when the detection of sparsely distributed GNPs within a small animal-sized imaging object is the prime concern. In practice, acquiring finer image resolution may not be the primary motivation of metal NP-based benchtop XFCT/XRF imaging applications, which are instead used to understand the molecular characteristics of the object of interest. On a related note, it is possible to deploy another pixelated detector coupled with a parallel-hole collimator, on the opposite side of the current detector location within our benchtop XFCT system. In that case, the overall image resolution will improve, along with further reduction of scan time/imaging.

Finally, the question remains as to whether the system sensitivity of our HEXITEC-based benchtop system could be enhanced further, while not increasing the XFCT scan time/dose. Throughout the current investigation, we made deliberate efforts to rival the system sensitivity achieved with our single crystal CdTe detector-based system. Due to several inherent differences (e.g., need for charge sharing correction for HEXITEC) between these two detector types, however, we were unable to perfectly achieve the goal (as can be inferred from the results based on 5 s data acquisition time). Apparently, our benchtop XFCT system described in this report is subject to further optimization efforts, in terms of both hardware and software aspects. Thus, we expect a good likelihood of further sensitivity improvement from the currently reported level, although we also anticipate a threshold for such improvement, which will have to be determined in future investigation.

V. CONCLUSION

In the current work, we successfully integrated a fully spectroscopic pixelated CdTe detector, HEXITEC, into our existing benchtop XFCT setup. We also demonstrated the capabilities of our upgraded benchtop XFCT system that were previously unachievable with our single crystal CdTe detector-based system. Specifically, adoption of HEXITEC with a custom-made parallel-hole collimator drastically reduced the XFCT scan time/dose, by up to a factor of 5, while achieving comparable system sensitivity under similar experimental conditions. Further scan time/dose reduction (by additional 5 folds or more) from the currently reported level would be readily achievable with the deployment of a larger FOV HEXITEC. Overall, the current work established the feasibility of benchtop XFCT imaging of small animal-sized objects containing biologically relevant GNP concentrations (on the order of 0.1 mg Au/cm^3 or 100 parts-per-million/ppm), with the scan time (on the order of 1 minute)/x-ray dose (on the order of 10 cGy) deemed acceptable for routine preclinical imaging applications. Despite the need for further improvement, the currently achieved combination of XFCT scan time, x-ray dose, and GNP detection limit, along with the demonstration of volumetric XFCT scans followed by XFCT image reconstruction in 3D, were unprecedented, to the best of our knowledge.

ACKNOWLEDGMENT

The authors acknowledge Md Ahmed, Ph.D., Liam O'Ryan, Ph.D., and Yonggang Cui, Ph.D. for their help during the currently described phantom imaging experiment. The authors also acknowledge Tamara Locke from Research Medical Library at the MD Anderson Cancer Center (MDACC) for her editorial help with the manuscript. The authors thank the High-Performance Research Computing Center, MDACC, for providing computational resources.

This work was supported by NIH under Award R01EB020658.

Biographies

SANDUN JAYARATHNA received the Ph.D. degree in high-energy physics from the University of Houston, Houston, TX, USA, in 2015. His Ph.D. work was in collaboration with the ALICE experiment at CERN, Geneva, Switzerland. Then, he worked as a Postdoctoral Fellow/a Research Engineer at The University of Texas MD Anderson Cancer Center, Houston, TX. He completed his medical physics residency training at The University of Kansas Medical Center, Kansas City, KS, USA.

HEM MOKTAN received the Ph.D. degree in biological physics from Oklahoma State University, OK, USA, in 2017, and worked as a Postdoctoral Fellow/a Research Engineer at The University of Texas MD Anderson Cancer Center, Houston, TX, USA. He is currently working as a Resident Medical Physicist with The University of Kansas Medical Center, Kansas City, KS, USA.

SANG HYUN CHO received the Ph.D. degree in nuclear engineering/medical physics from Texas A&M University, College Station, TX, USA, in 1997. He is currently working as a Professor with The University of Texas MD Anderson Cancer Center, Houston, TX, USA.

REFERENCES

[1]. Boisseau P, "Determination of three dimensional trace element distributions by the use of monochromatic X-ray microbeams," Ph.D. thesis, Dept. Phys., Massachusetts Inst. Technol., Cambridge, MA, USA, 1986.

[2]. Cesareo R and Mascarenhas S, "A new tomographic device based on the detection of fluorescent X-rays," Nucl. Instrum. Methods Phys. Res. A, Accel. Spectrom. Detect. Assoc. Equip, vol. 277, nos. 2–3, pp. 669–672, May 1989, doi: 10.1016/0168-9002(89)90802-4.

[3]. Cesareo R and Viezzoli G, "Trace element analysis in biological samples by using XRF spectrometry with secondary radiation," Phys. Med. Biol, vol. 28, no. 11, pp. 1209–1218, Nov. 1983, doi: 10.1088/0031-9155/28/11/002. [PubMed: 6657741]

[4]. Takeda T, Momose A, Yu Q, Yuasa T, Dilmanian FA, Akatsuka T, and Itai Y, "New types of X-ray computed tomography (CT) with synchrotron radiation: Fluorescent X-ray CT and phase-contrast X-ray CT using interferometer," Cell Mol. Biol, vol. 46, no. 6, pp. 1077–1088, Sep. 2000. [PubMed: 10976865]

[5]. Cheong SK, Jones BL, Siddiqi AK, Liu F, Manohar N, and Cho SH, "X-ray fluorescence computed tomography (XFCT) imaging of gold nanoparticle-loaded objects using 110 kVp X-rays," Phys. Med. Biol, vol. 55, no. 3, pp. 647–662, Feb. 2010, doi: 10.1088/0031-9155/55/3/007. [PubMed: 20071757]

[6]. Kuang Y, Pratx G, Bazalova M, Meng B, Qian J, and Xing L, "First demonstration of multiplexed X-ray fluorescence computed tomography (XFCT) imaging," IEEE Trans. Med. Imag, vol. 32, no. 2, pp. 262–267, Feb. 2013, doi: 10.1109/Tmi.2012.2223709.

[7]. Kuang Y, Pratx G, Bazalova M, Qian J, Meng B, and Xing L, "Development of XFCT imaging strategy for monitoring the spatial distribution of platinum-based chemodrugs: Instrumentation and phantom validation," Med. Phys, vol. 40, no. 3, Mar. 2013, Art. no. 030701, doi:10.1118/1.4789917.

[8]. Manohar N, Reynoso FJ, Diagaradjane P, Krishnan S, and Cho SH, "Quantitative imaging of gold nanoparticle distribution in a tumor-bearing mouse using benchtop X-ray fluorescence computed tomography," Sci. Rep, vol. 6, no. 1, pp. 1–10, Feb. 2016, doi: 10.1038/srep22079. [PubMed: 28442746]

[9]. Manohar N, Reynoso FJ, and Cho SH, "Technical note: A benchtop cone-beam X-ray fluorescence computed tomography (XFCT) system with a high-power X-ray source and transmission CT imaging capability," Med. Phys, vol. 45, no. 10, pp. 4652–4659, Oct. 2018, doi: 10.1002/mp.13138. [PubMed: 30125950]

[10]. Dunning CAS and Bazalova-Carter M, "Sheet beam X-ray fluorescence computed tomography (XFCT) imaging of gold nanoparticles," Med. Phys, vol. 45, no. 6, pp. 2572–2582, 2018, doi: 10.1002/mp.12893. [PubMed: 29604070]

[11]. Jones BL, Manohar N, Reynoso F, Karellas A, and Cho SH, "Experimental demonstration of benchtop X-ray fluorescence computed tomography (XFCT) of gold nanoparticle-loaded objects using lead- and tin-filtered polychromatic cone-beams," Phys. Med. Biol, vol. 57, no. 23, pp. N457–N467, Dec. 2012, doi: 10.1088/0031-9155/57/23/N457. [PubMed: 23135315]

[12]. Zhang S, Li L, Chen J, Chen Z, Zhang W, and Lu H, "Quantitative imaging of Gd nanoparticles in mice using benchtop cone-beam X-ray fluorescence computed tomography system," Int. J. Mol. Sci, vol. 20, no. 9, p. 2315, May 2019, doi: 10.3390/ijms20092315.

[13]. Li L, Zhang S, Li R, and Chen Z, "Full-field fan-beam X-ray fluorescence computed tomography with a conventional X-ray tube and photon-counting detectors for fast nanoparticle bioimaging," Opt. Eng, vol. 56, no. 4, Apr. 2017, Art. no. 043106, doi: 10.1117/1.Oe.56.4.043106.

[14]. Jung S, Kim T, Lee W, Kim H, Kim HS, Im H-J, and Ye S-J, "Dynamic *in vivo* X-ray fluorescence imaging of gold in living mice exposed to gold nanoparticles," IEEE Trans. Med. Imag, vol. 39, no. 2, pp. 526–533, Feb. 2020, doi: 10.1109/Tmi.2019.2932014.

[15]. Schuemann J, "Roadmap for metal nanoparticles in radiation therapy: Current status, translational challenges, and future directions," Phys. Med. Biol, vol. 65, no. 21, Oct. 2020, Art. no. 21RM02, doi: 10.1088/1361-6560/ab9159.

[16]. Jayarathna S, Ahmed MF, O'ryan L, Moktan H, Cui Y, and Cho SH, "Characterization of a pixelated cadmium telluride detector system using a polychromatic X-ray source and gold nanoparticle-loaded phantoms for benchtop X-ray fluorescence imaging," IEEE Access, vol. 9, pp. 49912–49919, 2021, doi: 10.1109/Access.2021.3069368. [PubMed: 33996343]

[17]. Seller P, Bell S, Cernik RJ, Christodoulou C, Egan CK, Gaskin JA, Jacques S, Pani S, Ramsey BD, Reid C, Sellin PJ, Scuffham JW, Speller RD, Wilson MD, and Veale MC, "Pixellated Cd(Zn)Te high-energy X-ray instrument," J. Instrum, vol. 6, no. 12, Dec. 2011, Art. no. C12009, doi: 10.1088/1748-0221/6/12/C12009.

[18]. Veale MC, Bell SJ, Seller P, Wilson MD, and Kachkanov V, "X-ray micro-beam characterization of a small pixel spectroscopic CdTe detector," J. Instrum, vol. 7, no. 7, Jul. 2012, Art. no. P07017, doi: 10.1088/1748-0221/7/07/P07017.

[19]. Ahmed MF, Yasar S, and Cho SH, "A Monte Carlo model of a benchtop X-ray fluorescence computed tomography system and its application to validate a deconvolution-based X-ray fluorescence signal extraction method," IEEE Trans. Med. Imag, vol. 37, no. 11, pp. 2483–2492, Nov. 2018, doi: 10.1109/Tmi.2018.2836973.

[20]. Cherry SR, Sorenson JA, and Phelps ME, Physics in Nuclear Medicine, 4th ed. Amsterdam, The Netherlands: Elsevier, 2012.

[21]. Veale MC, Bell SJ, Duarte DD, Schneider A, Seller P, Wilson MD, and Iniewski K, "Measurements of charge sharing in small pixel CdTe detectors," Nucl. Instrum. Methods Phys. Res. A, Accel. Spectrom. Detect. Assoc. Equip, vol. 767, pp. 218–226, Dec. 2014, doi: 10.1016/j.nima.2014.08.036.

[22]. Ma CM, "AAPM protocol for 40–300 kV X-ray beam dosimetry in radiotherapy and radiobiology," Med. Phys, vol. 28, no. 6, pp. 868–893, Jun. 2001, doi: 10.1118/1.1374247. [PubMed: 11439485]

[23]. Manohar N, Reynoso FJ, and Cho SH, "Experimental demonstration of direct L-shell X-ray fluorescence imaging of gold nanoparticles using a benchtop X-ray source," Med. Phys, vol. 40, no. 8, Aug. 2013, Art. no. 080702, doi: 10.1118/1.4816297.

[24]. Manohar N, Reynoso F, Jayarathna S, Moktan H, Ahmed MF, Diagaradjane P, Krishnan S, and Cho SH, "High-sensitivity imaging and quantification of intratumoral distributions of gold nanoparticles using a benchtop X-ray fluorescence imaging system," Opt. Lett, vol. 44, no. 21, pp. 5314–5317, Nov. 2019, doi: 10.1364/Ol.44.005314. [PubMed: 31674996]

[25]. Rose A, Vision: Human and Electronic. New York, NY, USA: Plenum Press, 1973.

[26]. Jowitt L, Wilson M, Seller P, Angelsen C, Wheater RM, Cline B, Schöne D, Lauba F, Goede M, Ball R, Verhoeven M, Gottseleben G, Boone MN, Van Assche F, and Veale MC, "HEXITEC 2 × 2 tiled hard X-ray spectroscopic imaging detector system," J. Instrum, vol. 17, no. 1, Jan. 2022, Art. no. P01012, doi: 10.1088/1748-0221/17/01/P01012.

[27]. Moktan H, Ahmed MF, Jayarathna S, Deng L, and Cho SH, "Monte Carlo study of X-ray detection configurations for benchtop X-ray fluorescence computed tomography of gold nanoparticle-loaded objects," Phys. Med. Biol, vol. 65, no. 17, Aug. 2020, Art. no. 175010, doi: 10.1088/1361-6560/ab9774.

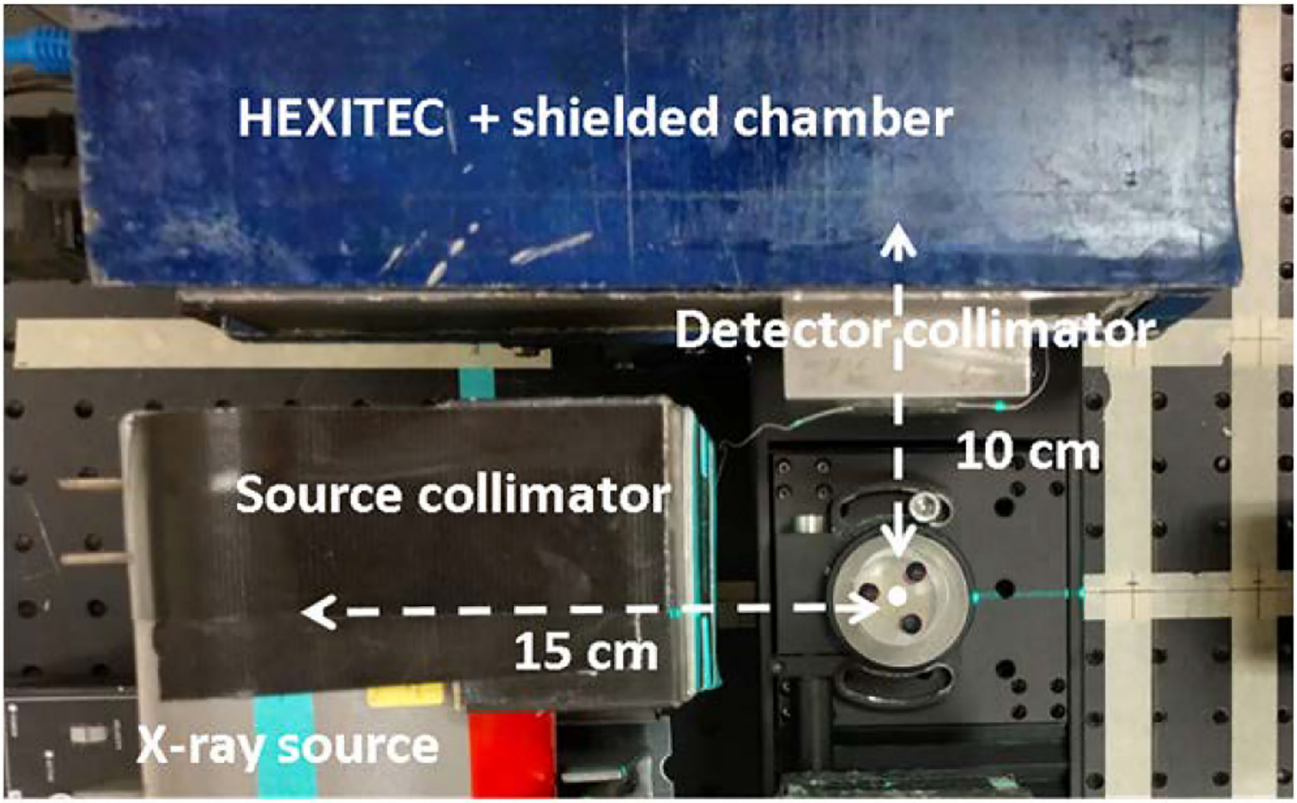

FIGURE 1.
Upgraded benchtop cone-beam XRF/XFCT imaging setup highlighting the major components, a 125-kVp x-ray source, source collimator, detector collimator, the HEXITEC system installed inside a shielded chamber, and the 3-hole phantom mounted on a rotational stage.

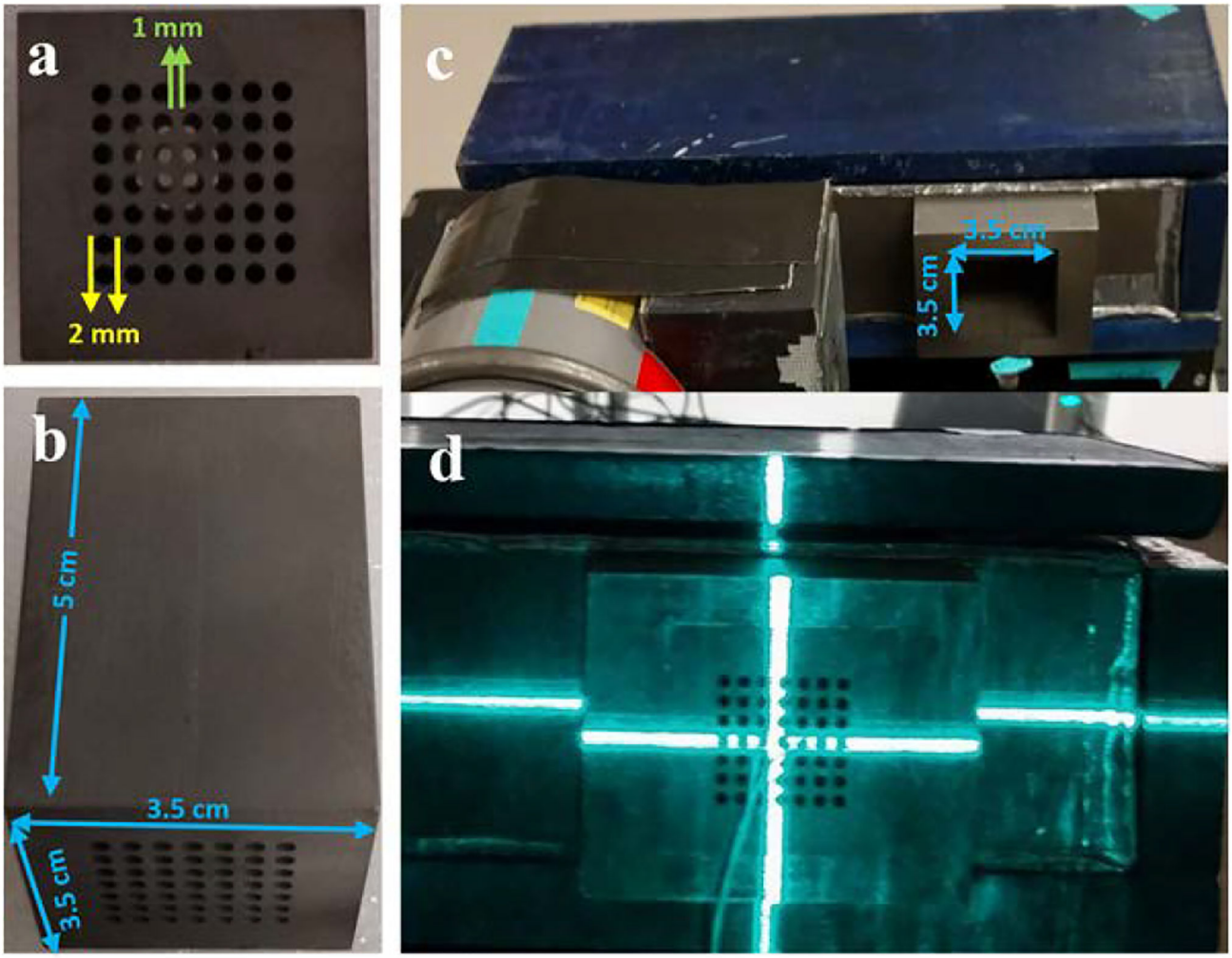

FIGURE 2.

2D parallel-hole detector collimator and XRF detection component. (a) The front elevation of the parallel-hole collimator has 2-mm-diameter holes drilled as a 7 × 7 array covering the 2 cm × 2 cm active area of the HEXITEC detector. (b) Top view of the collimator (3.5 cm × 3.5 cm × 5 cm). (c) Shielded chamber supporting both HEXITEC and detector collimator where the 3.5 cm × 3.5 cm collimator slot was engineered to facilitate the coupling of any type of external collimator with the detector. (d) Once the collimator was inserted into the slot, two laser beams were used to align it to the center of the phantom, where a laser crosshair was aligned with the x = 4 and y = 4 collimator hole in the array.

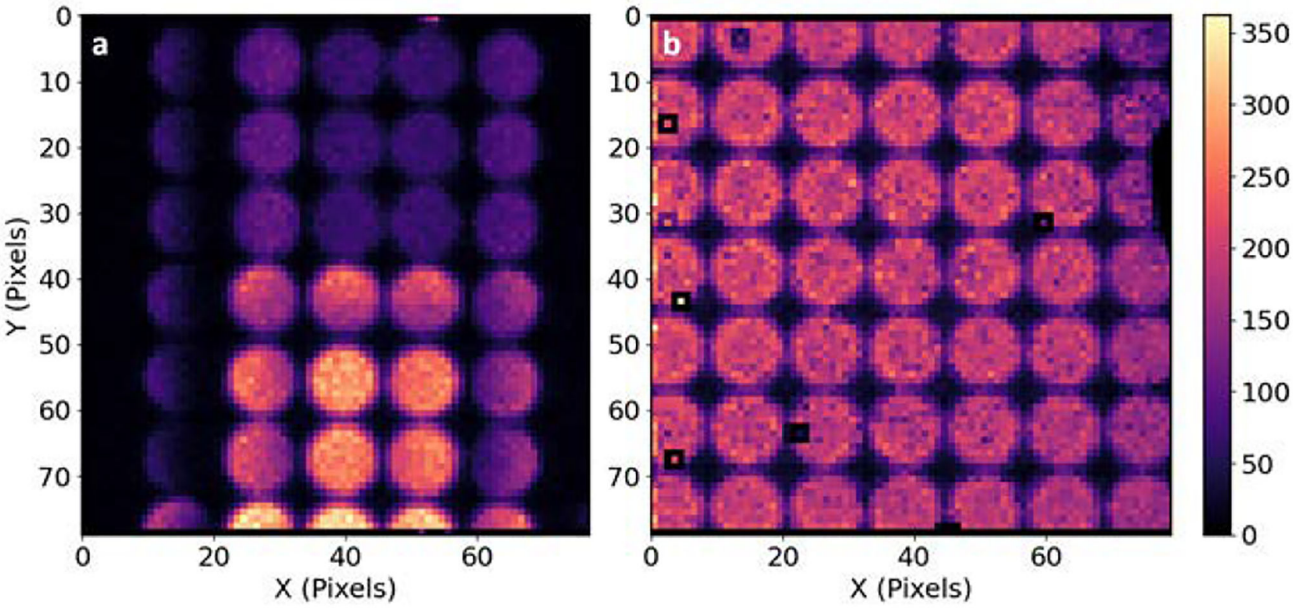

FIGURE 3.
2D images of (a) calibration and (b) imaging phantoms acquired with a built-in 2D imager in the HEXITEC software.

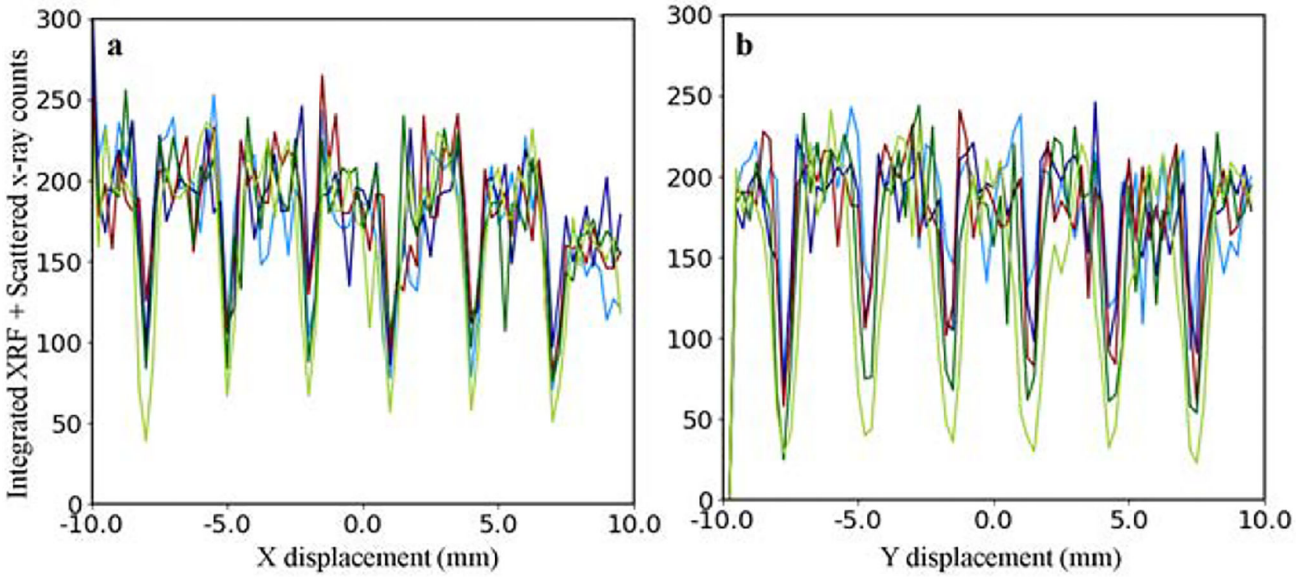

FIGURE 4.

Line profiles along the centrally located pixels (a) for y = 38, 39, 40, 41, and 42 with a clear 7 distinct spikes; (b) the same profiles are visible for x = 38, 39, 40, 41, and 42 with similar distinct spikes.

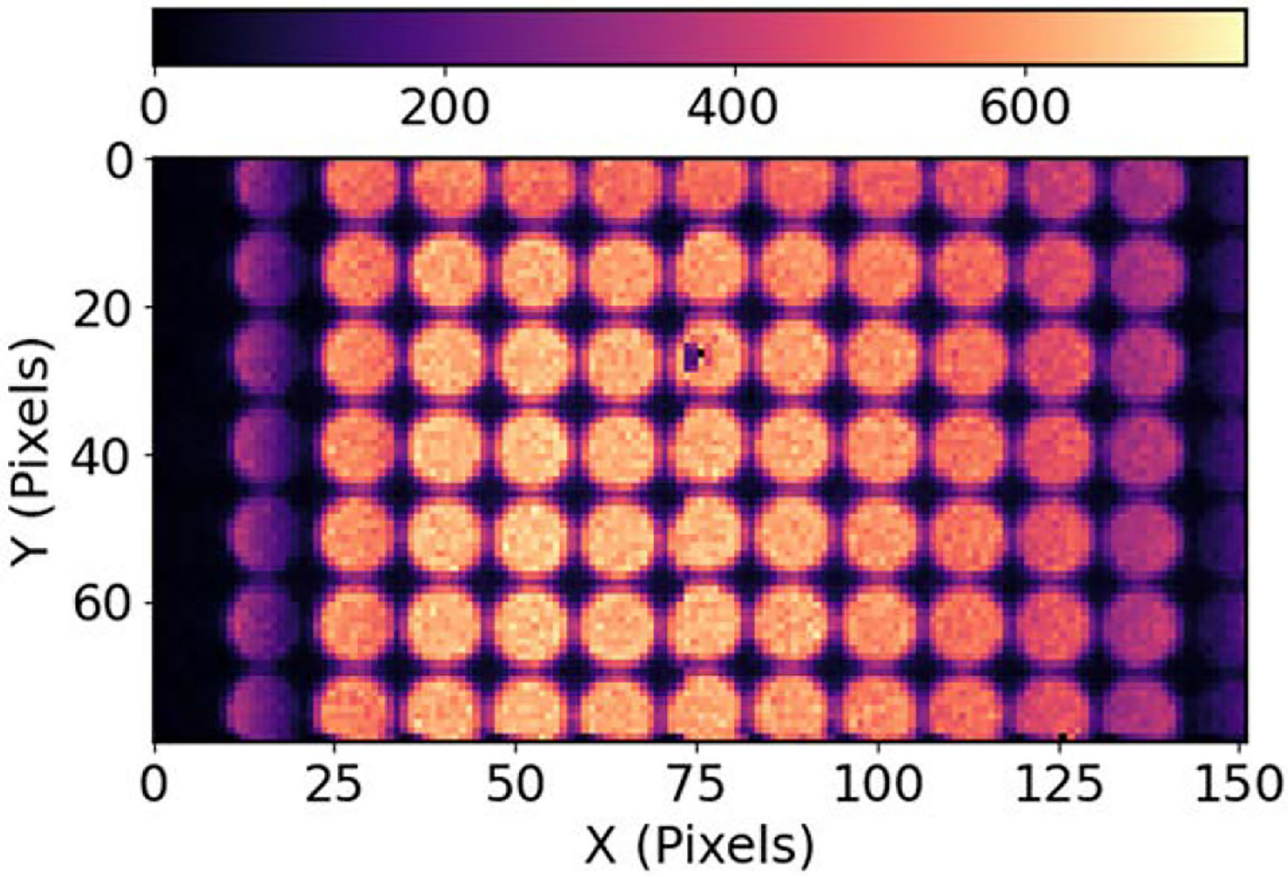

FIGURE 5.
2D image mimicking the expanded detector sensor area, obtained by translating the detector and combining the .hxt files from separate scans of left and right sides of the imaging phantom.

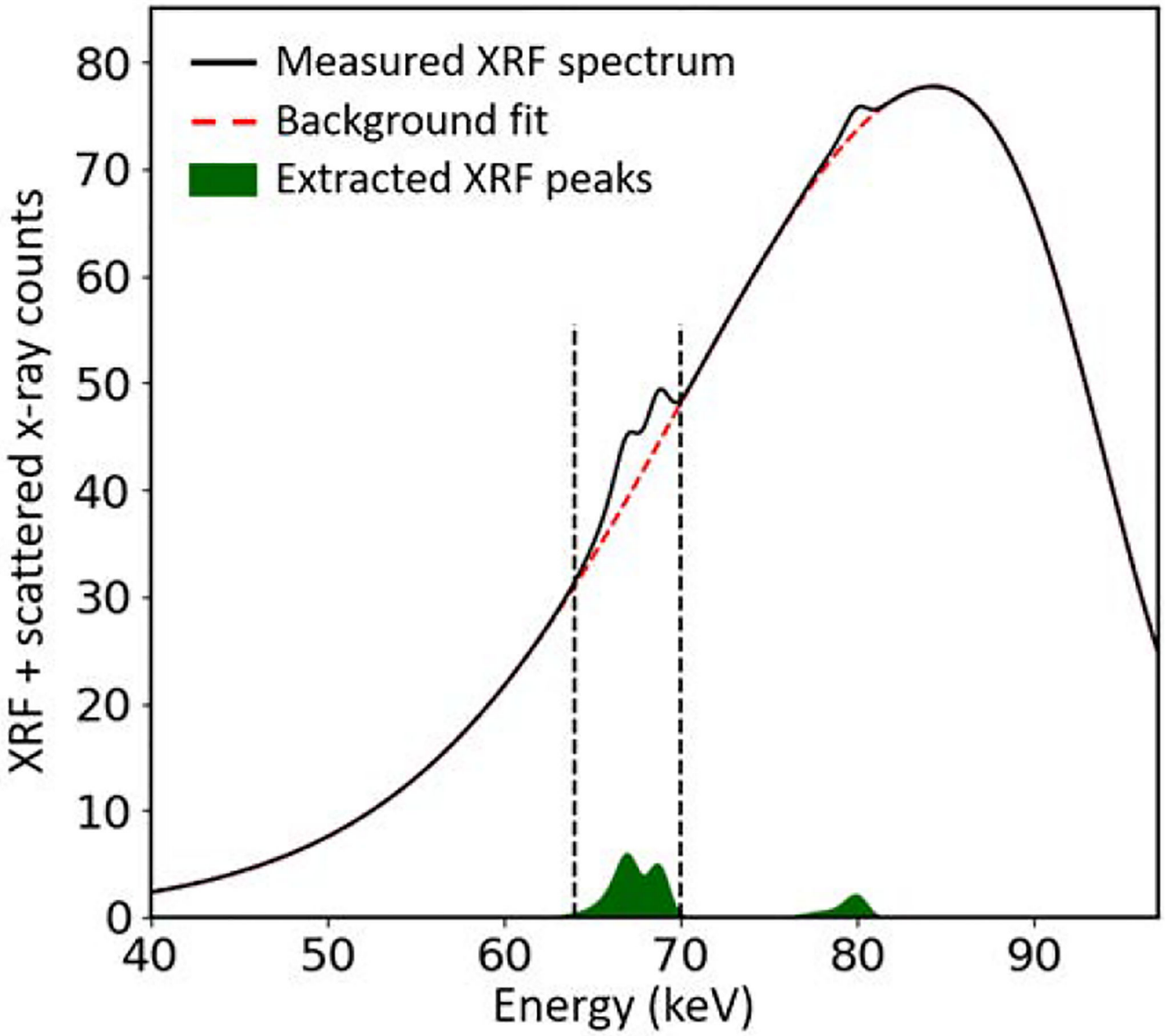

FIGURE 6.

Acquired XRF + scattered photon energy spectrum based on pixel-by-pixel spectrum merging using 10 × 10 pixels along with the deconvolution-based XRF signal extraction. The spectrum shown was obtained with 5 s data acquisition time for the calibration phantom filled with GNP solution at 0.05 mg Au/cm^3 concentration.

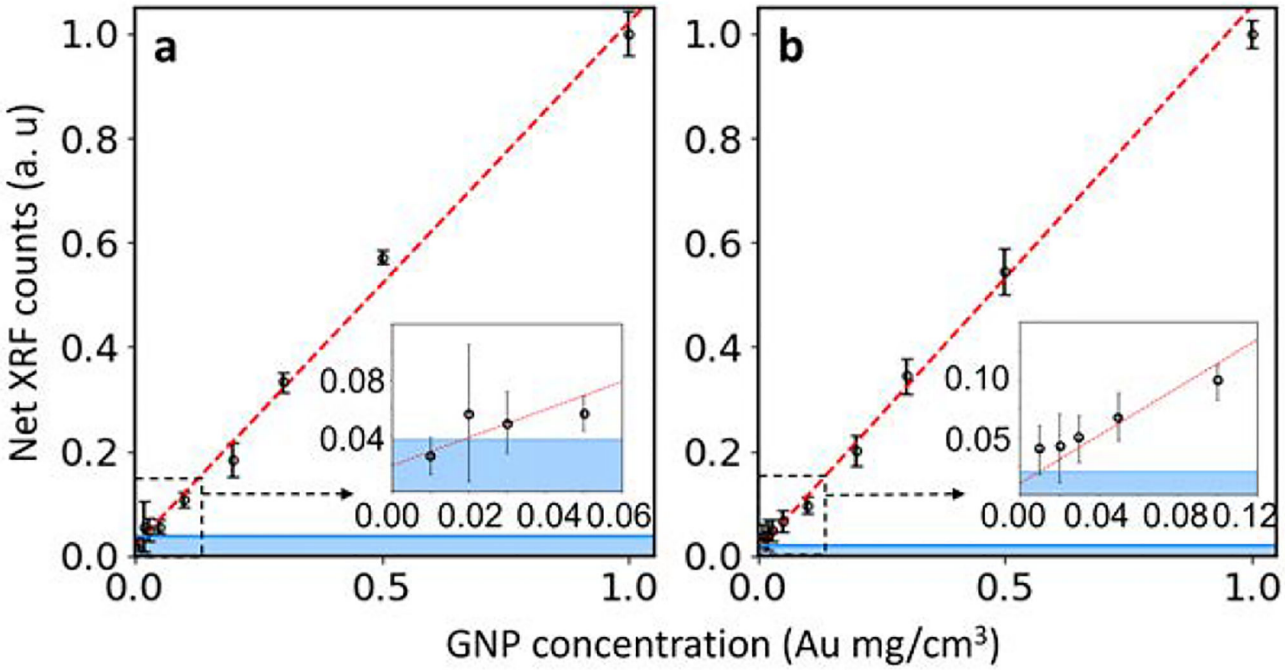

FIGURE 7.

The calibration curves for the current benchtop XFCT configuration with acquisition time of (a) 5 s and (b) 10 s, respectively. The horizontal line shows the 1.96σ above the Compton background, below which XRF signal was considered undetectable. The zoomed view of the low concentration area below 0.1 mg Au/cm^3 for acquisition time of 5 s and 10 s are shown in respective inserts.

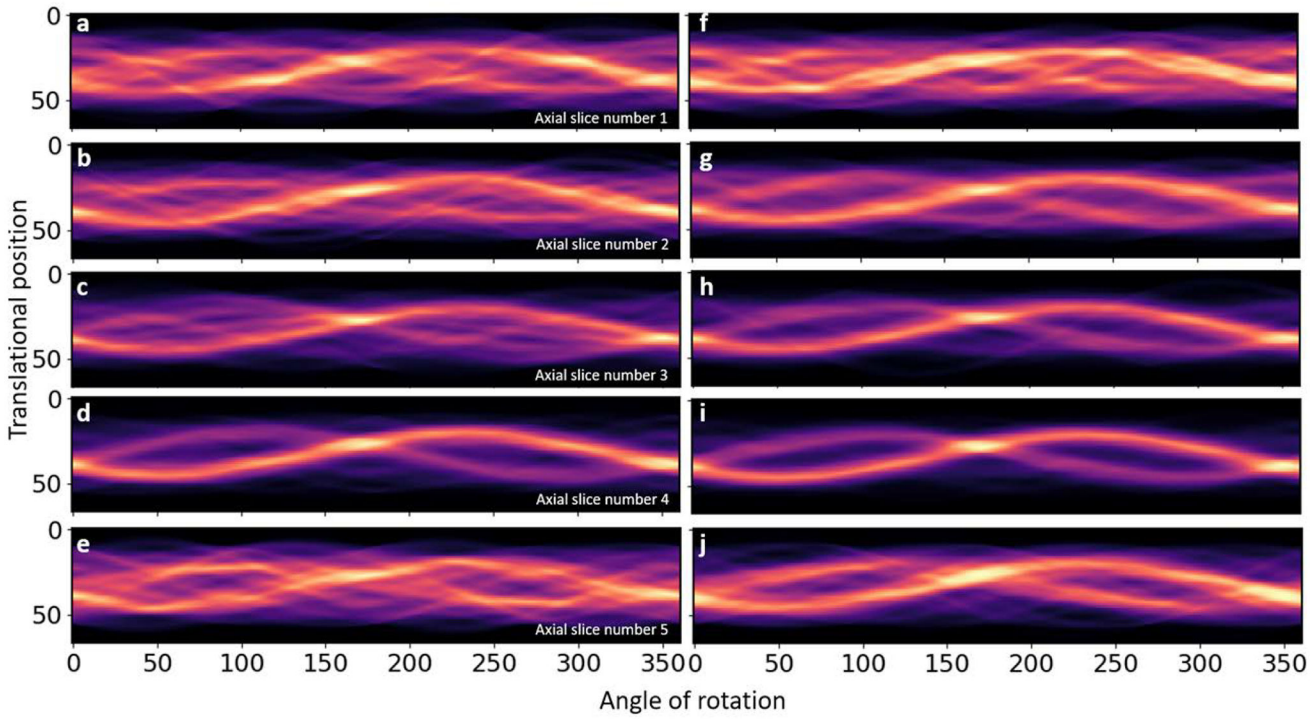

FIGURE 8.

Projection sinograms were obtained for slice numbers 1–5, based on data acquisition time of 5 s (a-e) and 10 s (f-j); no useful XRF signals were obtained for collimator rows 6 and 7, due to the length (15 mm) of the GNP-loaded column. The x axis represents the projection angle in degrees and y axis is the number of detector elements.

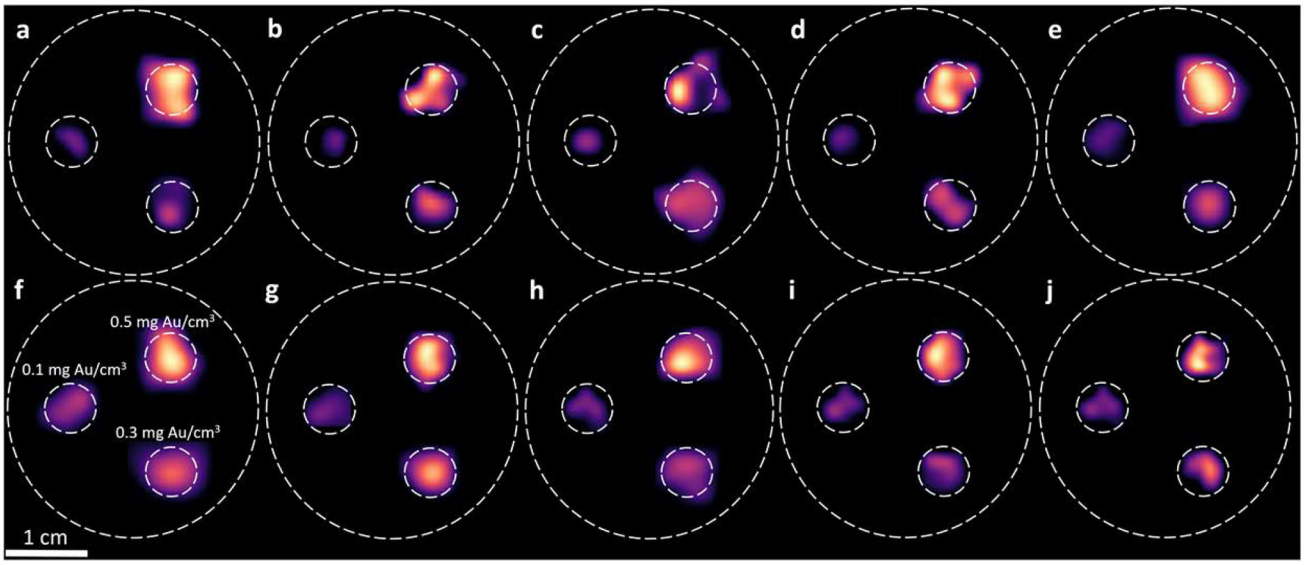

FIGURE 9.

The reconstructed axial images for slice numbers 1 through 5 for XFCT. Images based on XFCT scans with acquisition time of 5 s (a-e) and 10 s (f-j). Each GNP-filled region was demarcated inside the phantom by using a smaller circle for better visualization.

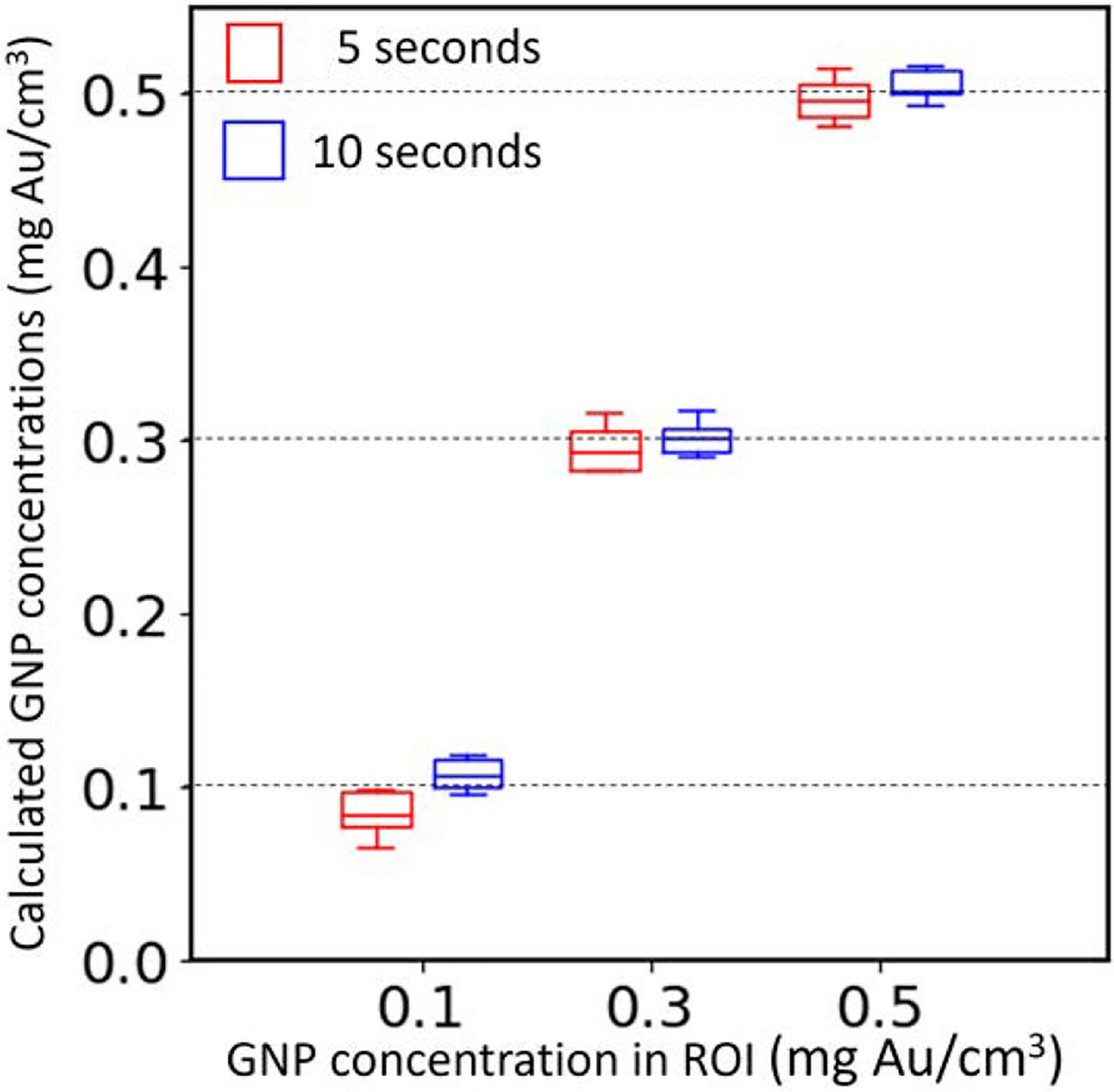

FIGURE 10.

The distribution of GNP concentrations derived from the reconstructed images for axial slices 1–5. The horizontal dashed lines represent the nominal/expected GNP concentrations inside the ROIs. For 5 s scan time the reconstructed concentrations found to be spread-out more compared to 10 s scan time.

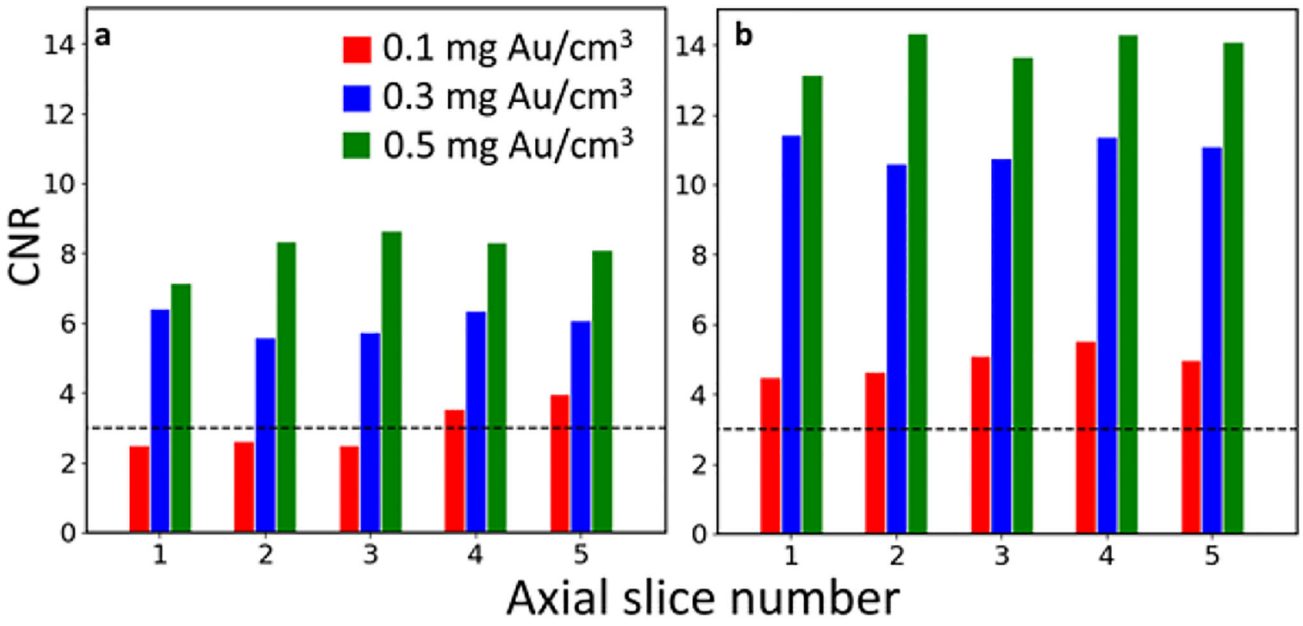

FIGURE 11.

The calculated CNR values for each axial slice in the reconstructed images based on (a) 5 s and (b) 10 s acquisition time. The horizontal dashed line shows the GNP detection threshold based on the Rose criterion, CNR = 3.

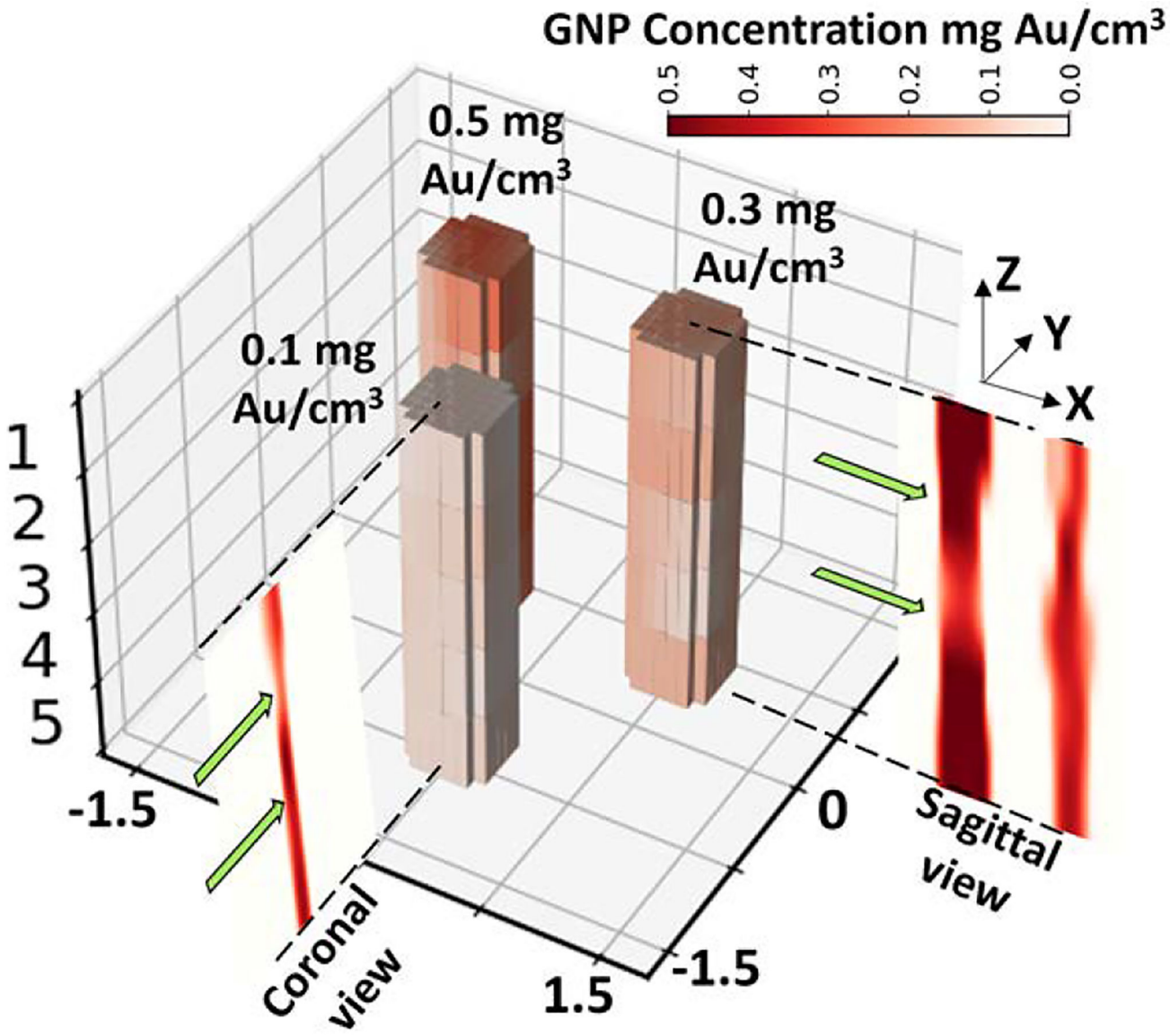

FIGURE 12.

Reconstructed 3D image from stacked axial slices, based on the XFCT scan with 5 s acquisition time. The image clearly shows all three GNP-loaded regions inside the imaging phantom. It also illustrates some local variation of GNP concentration in each region (shown by the green arrows). Additionally, it suggests some difficulty of imaging the 0.1 mg Au/cm^3 region with the 5 s scan. Here, z axis shows the reconstructed axial slice number and x-y plane represents the distance from the center of the phantom in ±cm.